

iPTF16geu: A multiply-imaged gravitationally lensed Type Ia supernova

A. Goobar,^{1*} R. Amanullah,¹ S. R. Kulkarni,² P. E. Nugent,^{3,4} J. Johansson,⁵
C. Steidel,² D. Law,⁶ E. Mörtzell,¹ R. Quimby,^{7,8} N. Blagorodnova,²
A. Brandeker,⁹ Y. Cao,¹⁰ A. Cooray,¹¹ R. Ferretti,¹ C. Fremling,¹² L. Hangard,¹
M. Kasliwal,² T. Kupfer,² R. Lunnan,^{2,9} F. Masci,¹³ A. A. Miller,^{15,16}
H. Nayeri,¹¹ J. D. Neill,² E. O. Ofek,⁵ S. Papadogiannakis,¹ T. Petrushevskaya,¹
V. Ravi,² J. Sollerman,¹² M. Sullivan,¹⁴ F. Taddia,¹² R. Walters,² D. Wilson,¹¹
L. Yan,² O. Yaron⁵

¹The Oskar Klein Centre, Physics Department, Stockholm University, Albanova University
Center, SE 106 91 Stockholm, Sweden,

²Cahill Center for Astrophysics, California Institute of Technology, Pasadena, CA 91125,
USA,

³Department of Astronomy, University of California, Berkeley, CA 94720-3411, USA,

⁴Lawrence Berkeley National Laboratory, 1 Cyclotron Road, MS 50B-4206, Berkeley, CA
94720, USA,

⁵Department of Particle Physics and Astrophysics, Weizmann Institute of Science, Rehovot
7610001, Israel,

⁶Space Telescope Science Institute, 3700 San Martin Drive, Baltimore, MD 21218, USA,

⁷Department of Astronomy, San Diego State University, San Diego, CA 92182, USA,

⁸Kavli IPMU (WPI), UTIAS, The University of Tokyo, Kashiwa, Chiba 277-8583, Japan,

⁹Department of Astronomy, Stockholm University, Albanova, SE 10691 Stockholm, Sweden,

¹⁰eScience Institute and Department of Astronomy, 3910 15th Ave NE Seattle, WA
98195-1570, USA,

¹¹Department of Physics & Astronomy, University of California, Irvine, CA 92697

¹²The Oskar Klein Centre, Astronomy Department, Stockholm University, Albanova
University Center, SE 106 91 Stockholm, Sweden,

¹³Infrared Processing and Analysis Center, California Institute of Technology, Pasadena, CA,
91125, USA,

¹⁴Department of Physics and Astronomy, University of Southampton, Southampton, SO17
1BJ, UK,

¹⁵Center for Interdisciplinary Exploration and Research in Astrophysics (CIERA) and
Department of Physics and Astronomy, Northwestern University, 2145 Sheridan Road,

Evanston, IL 60208, USA,

¹⁶ The Adler Planetarium, 1300 S. Lakeshore Drive, Chicago, IL 60605, USA

*To whom correspondence should be addressed; E-mail: ariel@fysik.su.se.

We report the discovery of a multiply-imaged gravitationally lensed Type Ia supernova, iPTF16geu, at redshift $z = 0.409$. This phenomenon could be identified because the light from the stellar explosion was magnified more than fifty times by the curvature of space around matter in an intervening galaxy.

We used high spatial resolution observations to resolve four images of the lensed supernova, approximately $0.3''$ from the center of the foreground galaxy. The observations probe a physical scale of ~ 1 kiloparsec, smaller than what is typical in other studies of extragalactic gravitational lensing. The large magnification and symmetric image configuration implies close alignment between the line-of-sight to the supernova and the lens. The relative magnifications of the four images provide evidence for sub-structures in the lensing galaxy.

One of the foundations of Einstein’s theory of General Relativity is that matter curves the surrounding space-time. For the rare cases of nearly perfect alignment between an astronomical source, an intervening massive object and the observer, multiple images of a single source can be detected, a phenomenon known as strong gravitational lensing.

Although many strongly lensed galaxies and quasars have been detected to date, it has proved extremely difficult to find multiply-imaged lensed supernova (SN) explosions. Type Ia supernovae (SNe Ia) are particularly interesting sources due to their “standard candle” nature. These explosions have nearly identical peak luminosity which makes them excellent distance indicators in cosmology (*I*). For lensed SNe Ia, the standard candle property allows the flux magnification to be estimated directly, independent of any model related to the lensing

galaxy (2, 3). This removes important degeneracies in gravitational lensing measurements, the mass-sheet degeneracy (4) and the source-plane degeneracy (5).

A lensed SN Ia at redshift $z = 1.388$ with a large amplification ($\mu \sim 30$), PS1-10afx, where multiple images could have been expected, has been reported earlier (6). A foreground lens was later identified at $z = 1.117$ (7). However, at the time of the discovery several interpretations were discussed, including a super-luminous supernova (8). Since the lensed SN Ia hypothesis was only accepted long after the explosion had faded, no high spatial resolution imaging could be carried out in that case to verify the strong lensing nature of the system. Multiple-images of another supernova, SN Refsdal (9), were discovered in a Hubble Space Telescope (HST) survey of the massive galaxy cluster MACS J1149.6+2223. As the source was identified as a core-collapse supernova it could not be used to measure the lensing magnification directly.

Thanks to the well-known characteristics of their time-dependent brightness in optical and near-infrared filters (the SN lightcurves), multiply-imaged SNe Ia are also ideally suited to measure time-delays in the arrival of the images. This provides a direct probe of the Hubble constant, the cosmological parameter measuring the expansion rate of the universe (10), as well as leverage for studies of dark energy (11, 12), the cosmic constituent responsible for the accelerated expansion of the universe.

The intermediate Palomar Transient Factory (iPTF) searches the sky for new transient phenomena at optical wavelengths. It uses image differencing between repeated observations (13) with a large field-of-view camera (7.3 sq.deg) at the 48-inch telescope (P48) at the Palomar Observatory (14). The first detection of iPTF16geu, with a statistical significance of five standard deviations (5σ), is from 2016 September 5. The new source was first recognized by a human scanner on September 11 (15). iPTF16geu (also known as SN 2016geu) was found near the center of the galaxy SDSS J210415.89-062024.7, at right ascension $21^h 4^m 15.86^s$ and declination $-6^\circ 20' 24.5''$ (J2000).

Spectroscopic identification was carried out with the Spectral Energy Distribution (SED) Machine (16) at the Palomar 60-inch telescope (P60) on 2016 October 2 and iPTF16geu was found to be spectroscopically consistent with a normal SN Ia at $z \approx 0.4$ (see Fig. 1). Further spectroscopic observations from the Palomar 200-inch telescope (P200) and the 2.5-meter Nordic Optical Telescope (NOT) were used to confirm the SN Ia identification and to establish the redshift of the host galaxy from narrow sodium (Na I D) absorption lines, as $z = 0.409$. The P200 and NOT spectra also show absorption features from the foreground lensing galaxy at $z = 0.216$. To estimate the velocity dispersion of the lensing galaxy, we fit two Gaussian functions with a common width to the $H\alpha$ and [N II] emission lines in the P200 spectrum in Fig 1D. After taking the instrumental resolution into account, we measure $\sigma = 3.6^{+0.9}_{-0.6} \text{ \AA}$, corresponding to a velocity dispersion of $\sigma_v = 163^{+41}_{-27} \text{ km s}^{-1}$.

Photometric observations of iPTF16geu collected at P48 and with the SED Machine Rainbow Camera (RC) at P60, between 2016 September 5 and October 13 (see Fig. 2), were used to estimate the peak flux and lightcurve properties of the SN with the SALT2 lightcurve fitting tool (17). The best fit lightcurve template, also shown in Fig. 2, confirms that the observed lightcurve shapes are consistent with a SN Ia at $z = 0.409$. These fits also indicate some reddening of the supernova, suggesting that iPTF16geu suffers from moderate extinction by dust. This produces dimming at optical wavelengths of 20-40%, with the largest losses in the g -band observations. Thanks to the standard candle nature of SNe Ia, after correcting the peak magnitude for lightcurve properties (18, 19), the flux of the SN was found to be ~ 30 standard deviations brighter than expected for the measured redshift. This suggested that iPTF16geu was gravitationally lensed and we estimated the lensing amplification to be $\mu \sim 52$. Expressed in astronomical magnitudes, $\Delta m = -4.3 \pm 0.2 \text{ mag}$, where the uncertainty is dominated by the brightness dispersion of normal SNe Ia. Since the magnification is derived from comparing the observed brightness of iPTF16geu to other SNe Ia (20) within a narrow redshift range around

$z = 0.409$, the measurement of the lensing magnification is independent of any assumptions on cosmology, e.g., the value of the Hubble constant or other cosmological parameters. The lensing magnification is also independent of a lens model, which is the only way to determine the magnification for almost all other strong lensing systems.

The optical observations from Palomar, with a typical angular resolution (atmospheric seeing) of $2''$, were insufficient to spatially resolve any multiple images that could result from the strong lensing nature of the system (Fig. 3A). We therefore obtained K_s -band ($2.2\ \mu\text{m}$) observations from the European Southern Observatory (ESO) with the Nasmyth Adaptive Optics System Near-Infrared Imager and Spectrograph (NACO) at the Very Large Telescope (VLT). An angular resolution of $\sim 0.3''$ (full-width half-max, FWHM) was obtained at the location of the target. Adaptive optics (AO) corrections of the seeing were performed using a natural bright star, $\sim 30''$ south-east of the SN location, indicated in Fig. 3 along with the SDSS pre-explosion image of the field (21).

The near-IR image from VLT indicated the structure expected in a strongly lensed system, with higher flux in the northeastern and southwestern regions of the system, compared to the center (Fig. 3B). Multiple images of the system were first resolved with observations from the Keck observatory at near-infrared wavelengths, using the Laser Guide Star aided Adaptive Optics (LGS AO) with the OH-Suppressing Infra-Red Imaging Spectrograph (OSIRIS) instrument, yielding an image quality of $0.07''$ FWHM in the H -band centered at $1.6\ \mu\text{m}$ (Fig. 3C).

LGS AO observations of iPTF16geu using the Near-InfraRed Camera 2 (NIRC2) at the Keck telescope on 2016 October 22 and November 5, in K_s -band and J -band ($1.1\ \mu\text{m}$) respectively, and optical images obtained with the Hubble Space Telescope (HST) on 2016 October 25, are shown in Fig. 4. The HST observations were carried out through the $F475W$, $F625W$ and $F814W$ filters, where the names correspond to the approximate location of the central wavelength in nanometers.

The observations exhibit four images of iPTF16geu, $0.26''$ – $0.31''$ from the center of the lensing galaxy, with nearly 90° azimuthal separations. The extended host galaxy, warped by the lens to form a partial Einstein ring, is brighter in the near-IR compared to the observations through optical filters. Thus, the fainter individual SN images are poorly resolved for the observations with the longest wavelengths in Fig. 4. Furthermore, the SN Ia spectral energy distribution (redshifted to $z = 0.4$) peaks within the $F625W$ and $F814W$ filters, see e.g. (22). Dimming by interstellar dust in the line of sight is roughly inversely proportional to wavelength in the optical and near-IR (23). The biggest impact from extinction by dust is therefore expected for the shortest wavelength, in $F475W$ filter observations, where the two faintest SN images cannot be detected above the background light. The low spatial resolution lightcurves in Fig. 2 are dominated by the two brightest SN images, labelled 1 and 2 in Fig. 4D. The $F625W$ – $F814W$ magnitude difference (color) of the resolved images measured with HST indicate small differences in relative extinction between the SN images, except for image 4, which appears to have about two magnitudes of additional dimming in $F814W$.

Unaccounted dimming of light by scattering on dust grains in the line of sight would lead to an underestimation of the lensing amplification. Including corrections for differential extinction in the intervening lensing galaxy between the SN images suggest a wider range for the lensing magnification of iPTF16geu, between -4.1 and -4.8 mag (24).

The SN multiple-image positions in Fig 4 were used to construct a lensing model, with an isothermal ellipsoid galaxy lens (25, 26) with ellipticity $\epsilon_e = 0.15 \pm 0.07$ and mass $M = (1.70 \pm 0.06) \cdot 10^{10} M_\odot$ inside an ellipse with major axis 1.13 kpc and minor axis 0.97 kpc. Details of the lensing model are presented in the Supplementary Material (24). The lens model can be independently verified through comparisons between the model-predicted and observed velocity dispersion of the lensing galaxy. From the model we derive an estimate, $\sigma_v^{\text{mod}} = 156 \pm 4$ km s $^{-1}$, in good agreement with the measured value of the velocity dispersion (Fig. 1D).

However, the adopted smooth isothermal ellipsoid lens model predicts brightness differences between the multiple SN images that are in disagreement with the observations. Including corrections for extinction in the resolved SN images in the $F814W$ filter, we find large discrepancies between the model and measured magnitude differences for the multiple images of iPTF16geu: $\Delta m_{1j}^{obs} - \Delta m_{1j}^{mod} = (-0.3, -1.6, -1.5)$ mag for $j = 2, 3$ and 4 , where the indices follow the numbering scheme adopted in Fig. 4. The observed discrepancy between the smooth model predictions for the SN images 1 and 2 compared to 3 and 4 (brighter by a factor 4 and 3, respectively), cannot be accounted for by time-delays between the images, as they are predicted to be < 35 hours (24). Graininess of the stellar distribution and dark matter sub-halos in the lens galaxy, in addition to the smooth mass profile, can cause variations to magnification without altering image locations. These milli- and micro-lensing effects (27, 28), small enough not to cause additional resolved image separations, offer a plausible explanation for the deviation from the smooth lens model.

Available forecasts for wide-field surveys (29) suggest that about one strongly lensed SN Ia could be expected in our survey, irrespectively of redshift and magnification, with approximately a 30% chance to be in a quad configuration. For an average ellipticity of the lenses $e = 0.3$ (29), only about 1% of the lensed SNe are expected to have $\mu \gtrsim 50$ (30). We have performed an independent rate estimate, with a somewhat simplified lensing simulation but including survey specific parameters, and confirm that the probability to detect and classify a highly magnified SN Ia like iPTF16geu does not exceed the few percent level (24).

iPTF16geu appears to be a rather unlikely event, unless the actual rate of very magnified SNe is higher than anticipated, e.g., if the contribution from lensing by any kind of sub-structures in galaxies is underestimated, or if we are otherwise lacking an adequate description of gravitational lensing at the ~ 1 kpc scale. The physical scale probed by the resolved images of iPTF16geu is comparable to the smallest of the 299 multiply-imaged lensed systems in the

Master Lens Database (31). Using the standard candle nature of SNe Ia we can more easily detect strongly lensed systems with sub-arcsecond angular separations, allowing exploration of the bending of light at scales $\lesssim 1$ kpc, an otherwise challengingly small distance in studies of gravitational lensing (32). As demonstrated with iPTF16geu, discovered while still brightening with a modest size telescope and sub-optimal atmospheric conditions, the locations of these rare systems can be identified in advance of extensive follow-up imaging at high spatial resolution.

References and Notes

1. A. Goobar, B. Leibundgut, *Annu. Rev. Nuc. Part. Sci.* **61**, 251 (2011).
2. T. S. Kolatt, M. Bartelmann, *Mon. Not. Roy. Astron. Soc.* **296**, 763 (1998).
3. M. Oguri, Y. Kawano, *Mon. Not. Roy. Astron. Soc.* **338**, L25 (2003).
4. E. E. Falco, M. V. Gorenstein, I. I. Shapiro, *Astrophys. J.* **289**, L1 (1985).
5. P. Schneider, D. Sluse, *Astron. Astrophys.* **559**, A37 (2013).
6. R. M. Quimby, *et al.*, *Astrophys. J.* **768**, L20 (2013).
7. R. M. Quimby, *et al.*, *Science* **344**, 396 (2014).
8. R. Chornock, *et al.*, *Astrophys. J.* **767**, 162 (2013).
9. P. L. Kelly, *et al.*, *Science* **347**, 1123 (2015).
10. S. Refsdal, *Mon. Not. R. Astron. Soc.* **128**, 307 (1964).
11. A. Goobar, E. Mörtzell, R. Amanullah, P. Nugent, *Astron. Astrophys.* **393**, 25 (2002).
12. S. H. Suyu, *et al.*, *Astrophys. J.* **766**, 70 (2013).

13. Y. Cao, P. E. Nugent, M. M. Kasliwal, *Publ. Astron. Soc. Pac.* **128**, 114502 (2016).
14. N. M. Law, *et al.*, *Publ. Astron. Soc. Pac.* **121**, 1395 (2009).
15. A. Goobar, *The Astronomer's Telegram* **9603**, 1 (2016).
16. A. Ritter, C. C. Ngeow, N. Konidaris, R. Quimby, S. Ben-Ami, *Contributions of the Astronomical Observatory Skalnat Pleso* **43**, 209 (2014).
17. J. Guy, *et al.*, *Astron. Astrophys.* **466**, 11 (2007).
18. M. M. Phillips, *Astrophys. J.* **413**, L105 (1993).
19. R. Tripp, *Astron. Astrophys.* **331**, 815 (1998).
20. M. Betoule, *et al.*, *Astron. Astrophys.* **568**, A22 (2014).
21. S. Alam, *et al.*, *Astrophys. J.* **219**, 12 (2015).
22. P. A. Mazzali, *et al.*, *Mon. Not. R. Astron. Soc.* **439**, 1959 (2014).
23. J. A. Cardelli, G. C. Clayton, J. S. Mathis, *Astrophys. J.* **345**, 245 (1989).
24. Materials and methods are available as supplementary materials on Science Online.
25. A. Kassiola, I. Kovner, *Liege International Astrophysical Colloquia*, J. Surdej, D. Fraipont-Caro, E. Gosset, S. Refsdal, M. Remy, eds. (1993), vol. 31 of *Liege International Astrophysical Colloquia*, p. 571.
26. R. Kormann, P. Schneider, M. Bartelmann, *Astron. Astrophys.* **284**, 285 (1994).
27. R. Kayser, S. Refsdal, *Nature* **338**, 745 (1989).
28. H. J. Witt, S. Mao, *Astrophys. J.* **429**, 66 (1994).

29. M. Oguri, P. J. Marshall, *Mon. Not. R. Astron. Soc.* **405**, 2579 (2010).
30. K.-H. Chae, *Mon. Not. R. Astron. Soc.* **346**, 746 (2003).
31. L. A. Moustakas, *et al.*, *Bull. Am. Astron. Soc.* (2012), vol. 219, p. 146.01. The Master Lens Database is available at <http://admin.masterlens.org>.
32. D. A. Goldstein, P. E. Nugent, *Astrophys. J.* **834**, L5 (2017).
33. O. Yaron, A. Gal-Yam, *Publ. Astron. Soc. Pac.* **124**, 668 (2012).
34. More information about the iPTF survey is available at <http://www.ptf.caltech.edu/iptf>.
35. E. O. Ofek, *et al.*, *Publ. Astron. Soc. Pac.* **124**, 854 (2012).
36. H. Brink, J. W. Richards, D. Poznanski, J. S. Bloom, J. Rice, S. Negahban, M. Wainwright, *Mon. Not. R. Astron. Soc.* **435**, 1047 (2013).
37. U. Rebbapragada, B. Bue, P. R. Wozniak, *Bull. Am. Astron. Soc.* (2015), vol. 225, p. 434.02.
38. F. J. Masci, *et al.*, *Publ. Astron. Soc. Pac.* **129**, 014002 (2017).
39. C. Fremling, *et al.*, *Astron. Astrophys.* **593**, A68 (2016).
40. J. B. Oke, J. E. Gunn, *Publ. Astron. Soc. Pac.* **94**, 586 (1982).
41. W. Freudling, *et al.*, *Astron. Astrophys.* **559**, A96 (2013).
42. J. Larkin, *et al.*, *Society of Photo-Optical Instrumentation Engineers (SPIE) Conference Series* (2006), vol. 6269 of *Proceedings of the Society of Photo-Optical Instrumentation Engineers Conference Series*, p. 62691A.
43. J. L. Sérsic, *Boletín de la Asociacion Argentina de Astronomia La Plata Argentina* **6**, 41 (1963).

44. R. Amanullah, *et al.*, *Mon. Not. R. Astron. Soc.* **453**, 3300 (2015).
45. P. A. R. Ade, *et al.*, *Astron. Astrophys.* **594**, A13 (2016).
46. C. R. Keeton, *ArXiv e-prints 0102340* (2001).
47. C. R. Keeton, *ArXiv e-prints 0102341* (2001).
48. P. Schneider, J. Ehlers, E. E. Falco, *Gravitational Lenses* (1992).
49. R. Pereira, *et al.*, *Astron. Astrophys.* **554**, A27 (2013).
50. A. Goobar, E. Mörtzell, R. Amanullah, M. Goliath, L. Bergström, T. Dahlén, *Astron. Astrophys.* **392**, 757 (2002).
51. J. F. Navarro, C. S. Frenk, S. D. M. White, *Astrophys. J.* **490**, 493 (1997).
52. V. Springel, *et al.*, *Mon. Not. Roy. Astron. Soc.* **391**, 1685 (2008).
53. G. Dobler, C. R. Keeton, *Astrophys. J.* **653**, 1391 (2006).
54. P. L. Schechter, D. Pooley, J. A. Blackburne, J. Wambsganss, *Astrophys. J.* **793**, 96 (2014).
55. J. Wambsganss, *Proceedings, 33rd Advanced Saas Fee Course on Gravitational Lensing: Strong, Weak, and Micro: Les Diablerets, Switzerland, April 7-12, 2003* (2006), pp. 453–540.
56. S. Ben-Ami, N. Konidaris, R. Quimby, J. T. Davis, C. C. Ngeow, A. Ritter, A. Rudy, *Ground-based and Airborne Instrumentation for Astronomy IV* (2012), vol. 8446 of *Proceedings of the Society of Photo-Optical Instrumentation Engineers Conference Series*, p. 844686.

AG and RA acknowledge support from the Swedish National Science Council (VR) and the Swedish National Space Board. EM acknowledge support from VR. The iPTF Swedish collaboration is funded through a grant from the Wallenberg foundation. We are grateful for support from the National Science Foundation through the PIRE GROWTH project, Grant No 1545949. Some of the data presented herein were obtained at the W.M. Keck Observatory, which is operated as a scientific partnership among the California Institute of Technology, the University of California and the National Aeronautics and Space Administration. The Observatory was made possible by the generous financial support of the W.M. Keck Foundation. The data presented here were obtained in part with ALFOSC, which is provided by the Instituto de Astrofísica de Andalucía (IAA) under a joint agreement with the University of Copenhagen and NOTSA. STSDAS and PyRAF are products of the Space Telescope Science Institute, which is operated by AURA for NASA. Part of the processing was carried out off-line using the commercial software package MATLAB and Statistics Toolbox Release 2013a, The MathWorks, Inc., Natick, Massachusetts, United States. Some of the data presented herein were obtained at the W.M. Keck Observatory, which is operated as a scientific partnership among the California Institute of Technology, the University of California and the National Aeronautics and Space Administration. The Observatory was made possible by the generous financial support of the W.M. Keck Foundation. All data used in this paper are made public, including the photometric data (tables S1, S2, S5) and spectroscopic data at public repository WISeREP (33) (<http://wiserep.weizmann.ac.il>). The positions of the SN images used in the lensing model are indicated in table S4.

SUPPLEMENTARY MATERIALS

www.sciencemag.org

Materials and Methods

Figs. S1, S2, S3

Tables S1, S2, S3, S4, S5, S6

References (34-56)

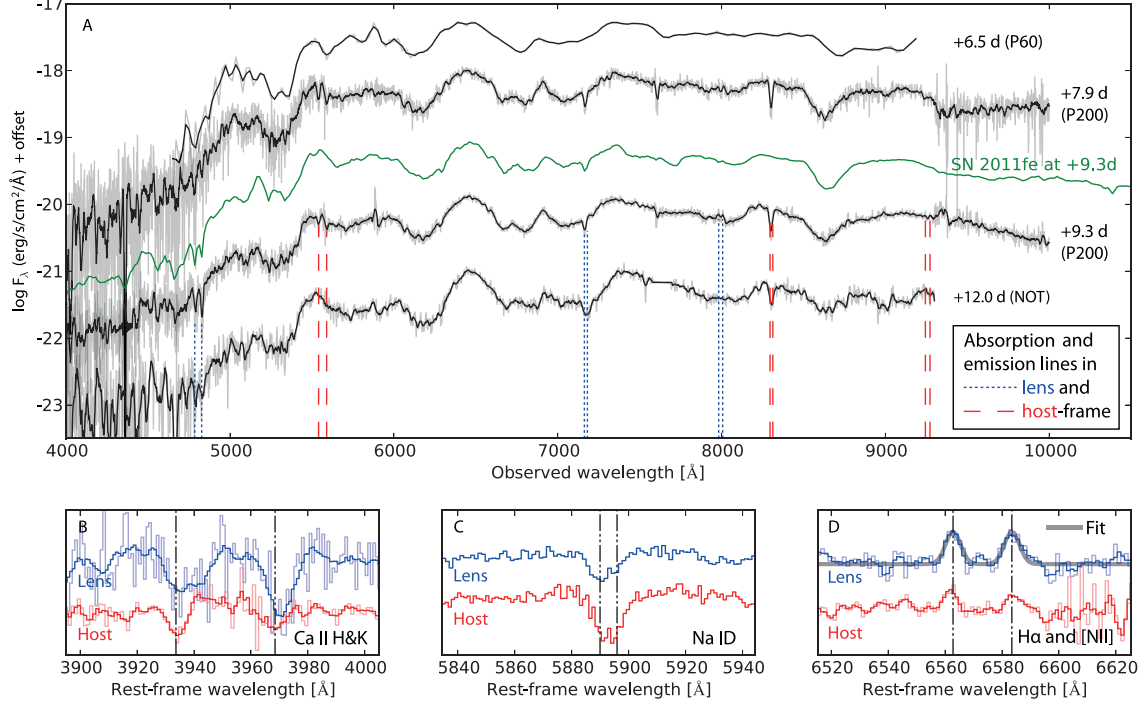


Figure 1: Spectroscopic identification of iPTF16geu as a Type Ia supernova and measurements of the redshifts of the SN host galaxy and the intervening lensing galaxy. Measurements of the SN spectral energy distribution, F_{λ} , obtained with the P60, P200 and NOT telescopes are best fitted by a normal SN Ia spectral template. Panel A shows a comparison with the near-by SN Ia, SN 2011fe, redshifted to $z = 0.409$ (green line, (22)) at a similar rest-frame phase, expressed in units of days with respect to the time of optical lightcurve maximum. The spectra also reveal narrow absorption and emission lines, marked by the dashed vertical lines, from which the redshifts of the lens ($z = 0.216$, blue lines) and SN host galaxy ($z = 0.409$, red lines) were determined. Zoomed in view in rest-frame wavelengths of the Ca II H & K and Na I D absorption features are shown in panels B, and C, respectively, together with the H α and [N II] emission lines (panel D). The H α and [N II] emission lines at $z = 0.216$ were used to fit the velocity dispersion of matter in the lensing galaxy, $\sigma_v = 163^{+41}_{-27}$ km s⁻¹.

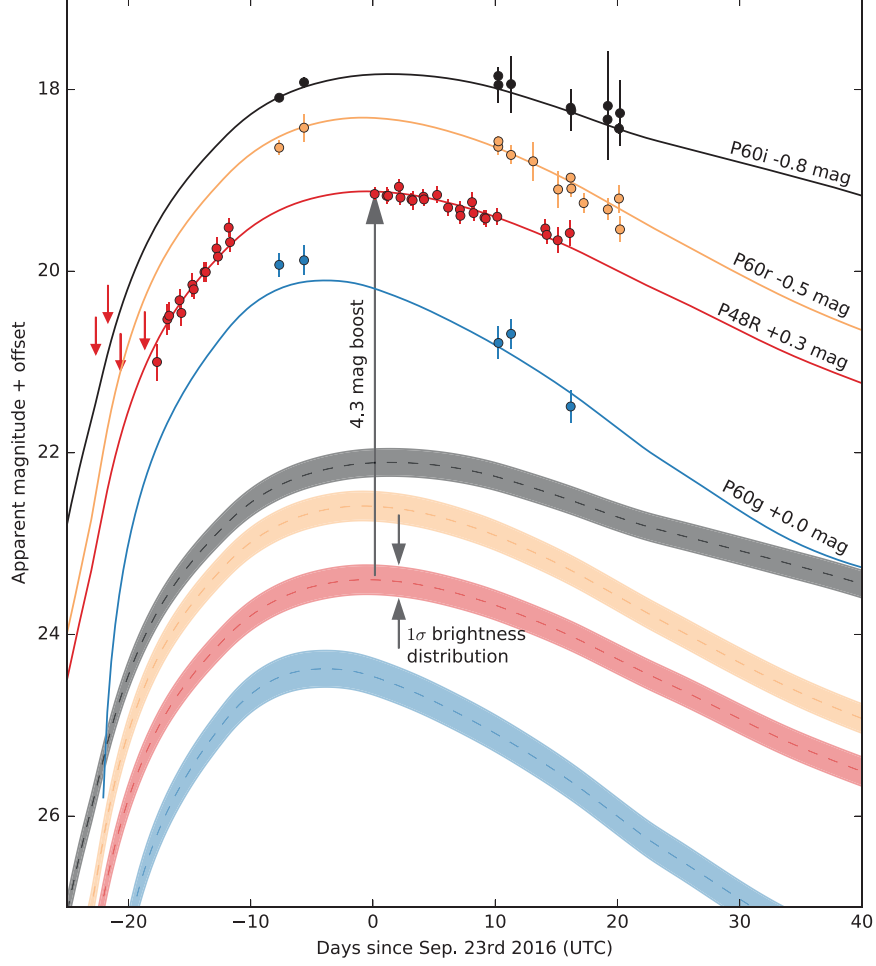


Figure 2: **Multi-color lightcurve of iPTF16geu showing that the supernova is 4.3 magnitudes (30 standard deviations) brighter than expected.** The magnitudes are measured with respect to time of maximum light (Modified Julian Date 57653.10) in R -band at P48 and g , r and i -band with RC on the SED Machine at P60. The filter transmission functions are shown in (24). The solid lines show the best fitted SALT2 (17) model to data. The dashed lines indicate the expected lightcurves at $z = 0.409$ (without lensing) where the bands represent the standard deviation of the brightness distribution for SNe Ia. In order to fit the observed lightcurves a brightness boost of 4.3 magnitudes is required.

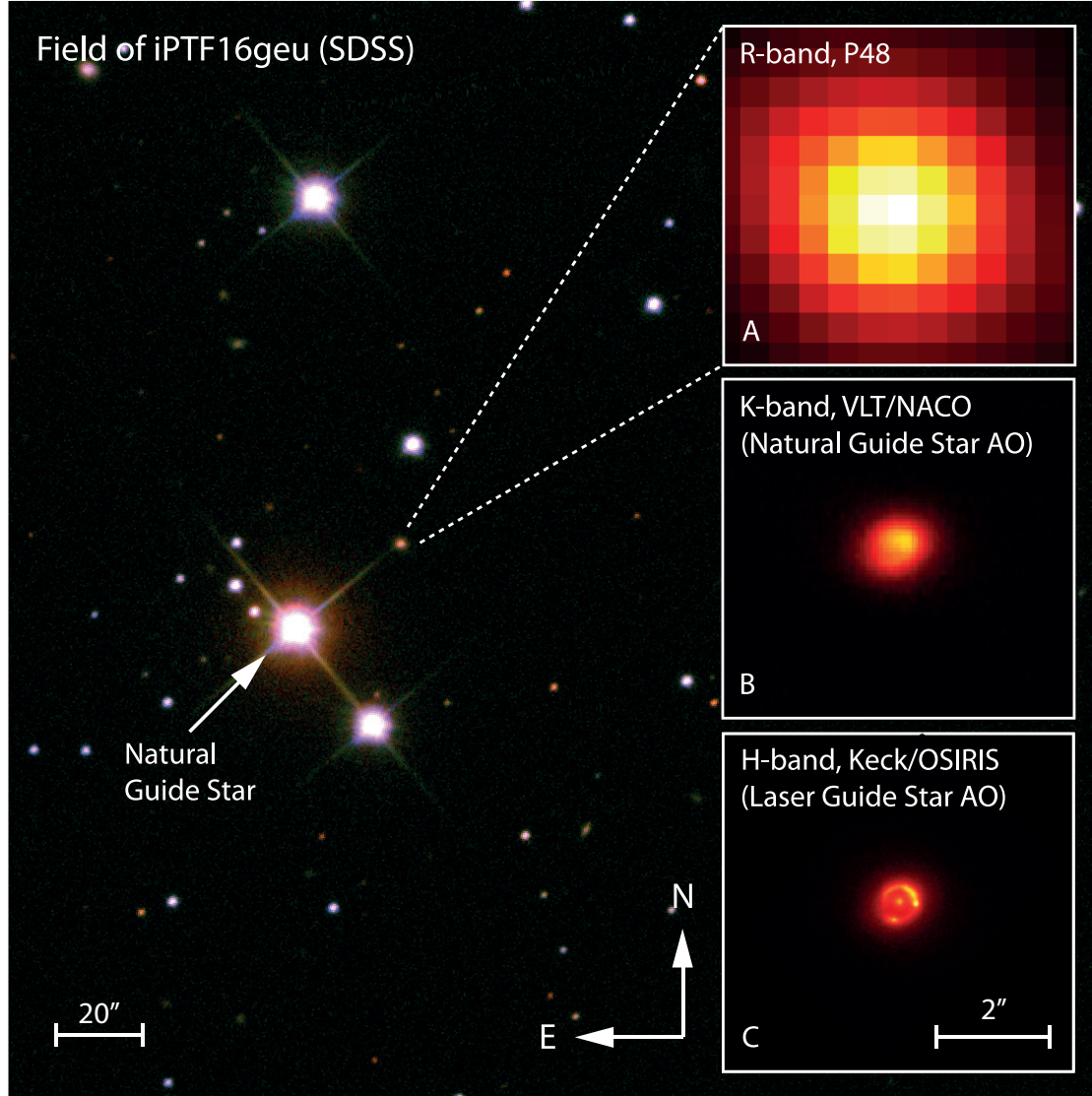


Figure 3: **Image of the field of iPTF16geu showing the spatial resolution of the ground based instruments used in this work.** A pre-explosion multicolor image from SDSS indicating the bright natural guide star and the position of the SN detection in R-band at P48 (zoomed in panel A) near the galaxy SDSS J210415.89-062024.7. The improved spatial resolution using a Natural star Guide System AO (NGSAO, panel B, and further using the Laser Star aided AO System (LGSAO, panel C) is shown.

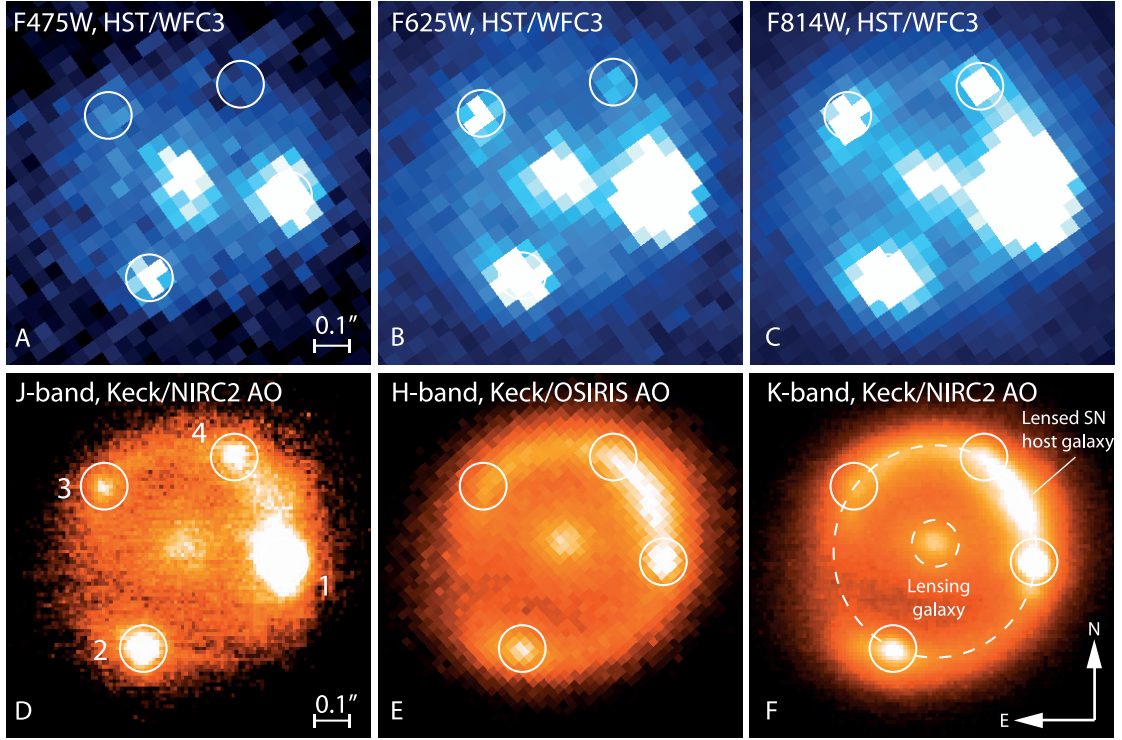


Figure 4: **High spatial resolution images from the Hubble Space Telescope and the Keck Observatory used to resolve the positions of the SN images, the partial Einstein ring of the host galaxy and the intervening lensing galaxy.** HST/WFC3 observations of iPTF16geu obtained on 2016 October 25 in the $F475W$, $F625W$ and $F814W$ bands. are shown in the panels A,B and C respectively. The images reveal four point sources, except for $F475W$ where SN images 3 and 4 are too faint. The NIR images obtained using Adaptive Optics aided Keck observations in the J , H and K_s bands are shown in panels D, E and F. All four SN images are clearly seen in J -band (panel D). For the H and K_s images, both the lensing galaxy at the center of the system and the lensed partial Einstein ring of the host galaxy are visible.

Supplementary Materials

Materials and Methods

Supernova survey and follow-up

Between late August and December 2016, the intermediate Palomar Transient Factory (34) has been performing a mixed-cadence experiment on the 48-inch Samuel Oschin Telescope (P48) at the Palomar Observatory searching for transient phenomena, e.g., supernovae. About 100 fields ($\simeq 700$ square degrees in sky area) were observed every night, while another 200 fields were observed every three nights. During a night, each field was visited twice, with a one hour interval. For fields with available SDSS *g*- and Mould *R*-band (35) reference images, these two visits were one in each filter. For fields with only *R*-band reference images, these two visits were both in the *R*-band.

Images were transferred and processed by our real-time image subtraction pipeline at the National Energy Research Scientific Computing Center (13). This pipeline, equipped with high-performance computing and machine-learning transient classifiers (36, 37), delivered transient candidates for visual inspection by our duty astronomers within ten minutes of images being taken.

On 2016 Sep 11, our duty astronomer identified a transient candidate near the core of the galaxy SDSS J210415.89-062024.7 in one *R*-band-only one-day cadence field. This candidate was saved as iPTF16geu (a.k.a. SN2016geu) and put in the queue for spectroscopic classifica-

tion. However, iPTF16geu was not observed spectroscopically until Oct 2, as described below, and both the redshift and the transient type were unknown until that point.

Meanwhile the field was observed with a daily cadence in the R -band, as listed in Table S1. Difference imaging photometry in R -band was obtained using the iPTF Discovery Engine at the Infrared Processing and Analysis Center (38, *IDE*), where reference images are aligned and matched to have the same point spread function (PSF) to the images where the SN is active. PSF photometry is then carried out and calibrated by matching the photometry of the field stars to the stellar catalog from the Sloan Digital Sky Survey (21, *SDSS*).

Complementary follow-up photometry, also listed in Table S1, was obtained in the $g'r'i'$ -bands with the Rainbow Camera (RC) on the Spectral Energy Distribution Machine (56, *SEDM*) mounted on the Palomar 60-inch telescope (P60). For the redshift of iPTF16geu, $z_{SN} = 0.409$, these filters provide an excellent match to the rest-frame UBV filters (Fig. S1) that have historically been used for studying SNe Ia. The RC data was pre-processed following standard photometry reduction techniques. The host subtraction was done by using the automatic reference-subtraction photometry pipeline `FPipe` (39). This is using a similar approach to *IDE*, but images from the Sloan Digital Sky Survey are used as reference images of the host galaxy since such data is not available from the RC. The photometric uncertainty is determined as the measured scatter from placing artificial PSFs in a circular pattern around the real transient and measuring their values on the subtracted images. The P48 and P60 photometry is listed in Table S2. In the table, only the statistical uncertainty of each data point is quoted. The systematic uncertainties are all subdominant in this analysis, since the error on the derived magnification will be dominated by the intrinsic SN Ia brightness uncertainty.

SEDM is a Caltech-developed instrument, designed for fast transient classification and follow-up. The SEDM focal plane combines a photometric instrument, the RC, and an Integral Field Unit (IFU) spectrograph. The focal plane of the RC is split into four quadrants, each

one containing a SDSS generation 2 filter: $u'g'r'i'$. The field of view (FoV) is 6.5 arcmin^2 for each filter. The IFU, a lenslet array, is mounted in the center. The instrument covers the optical range $4000\text{--}9500 \text{ \AA}$ with a constant wavelength resolving power of $R \simeq 100$, equivalent to a velocity resolution of 3000 km s^{-1} . Its FoV is 30 arcsec^2 and each spaxel covers an approximate diameter of $0.7''$. A spaxel is a spatial pixel that also contains a spectrum of its detected photons, which is characteristic for an IFU.

Spectroscopic follow-up

The first classification spectrum of iPTF16geu was obtained with the IFU on the SEDM on 2016 Oct 2. The combined spectrum (Fig. 1) consists of the average of two exposures, obtained with an offset of $10''$ to allow subtraction of the skylines. The data were reduced using a custom IFU pipeline developed for the instrument. Flux calibration and correction of telluric bands were done using the standard star BD+28 4211, which was taken at a similar airmass. An aperture of $4''$ was used to extract the spaxels. The details of all spectroscopic observations are listed in Table S3.

The classification and redshift of iPTF16geu from the low-resolution SEDM IFU spectrum was confirmed by observations obtained with the Double Spectrograph (40, DBSP) mounted on the Palomar 200-inch telescope (P200) and the ALFOSC instrument on the Nordic Optical Telescope (NOT).

For the DBSP observations the 600 lines/mm (with first order blaze wavelength 4000 \AA) grating was used with slitwidths $1.5''$ and $2''$ and the data were reduced with a custom pipeline written in the Interactive Data Language (IDL). Flux calibration and telluric correction were done with the flux standard star BD+28 4211.

For the ALFOSC spectrum grism #4 was used with the slitwidth $1.0''$. The data were reduced with a custom pipeline written in Matlab. Wavelength calibration was performed with a He-Ne

arc lamp, and flux calibration with the standard star BD+17 4708 observed the same night at similar airmass.

Adaptive Optics observations of iPTF16geu

Natural Guide Star Adaptive Optics imaging from the VLT

K_s -band observations were obtained on 2016 Oct 11 using the Nasmyth Adaptive Optics System with the Near-Infrared Imager and Spectrograph (NACO) at the Very Large Telescope (VLT). The bright star at R.A.= $21^{\circ}4'17.42''$ and Dec= $-6^{\circ}20'43.13''$, $29.5''$ south-east of iPTF16geu with $V = 11.5$ mag marked in Fig. 3, was used as a natural guide star (NGS). The spatial resolution decreases with the distance from the NGS, and $30''$ is close to the maximum distance for this technique. Due to problems with the visual wave-front sensor, the infrared wavefront sensor with the N20C80 dichroic was used. The observations were made with a standard jitter pattern in a $5''$ box with single exposure integrations of 20 s, saved in cube mode. In total, 348 frames were obtained. The data were reduced with the NACO `esorex` pipeline, using the standard jitter recipe (41). Since all exposures were individually saved, a small improvement in the final resolution could be obtained by selecting the best-resolved 20 % of the frames. The resulting image, Fig 3B, has an image quality of $\text{FWHM} \sim 0.3''$ at the location of the target, with a Strehl ratio of $\sim 5\%$. The Strehl ratio is defined as the ratio of peak diffraction intensities of an aberrated and a perfect wavefront. The ratio indicates the level of image quality in the presence of wavefront aberrations.

Laser Guide Star Adaptive Optics imaging from Keck

iPTF16geu was observed with the OSIRIS (42) imager behind the Keck I Laser Guide Star Adaptive Optics (LGSAO) system on 2016 Oct 13 and separately with the Keck II NIRC2 near-infrared imager in the H and K_s -bands (at $1.6 \mu\text{m}$ and $2.2 \mu\text{m}$ respectively) on 2016 Oct 22 and 23, and then again in the J -band (at $1.2 \mu\text{m}$) on Nov 05. The field of view of the OSIRIS

imager is $20'' \times 20''$ and is sampled with $0.02''$ pixels by a 1024×1024 Hawaii 1 HgCdTe array. The observation consisted of a sequence of 36 exposures of 30 s each in the OSIRIS “ H_{bb} ” filter ($1.638/0.330 \mu\text{m}$), dithered in a 3×3 box pattern with $2.5''$ separation. The NGS south-east of iPTF16geu mentioned above was used for tip/tilt correction. Immediately following the iPTF16geu observation, the tip/tilt star was centered on the OSIRIS imager and a short sequence of dithered observations was taken as a PSF reference, yielding point source $\text{FWHM} \simeq 0.07''$ (as measured from the $H = 15$ mag star at R.A. = $21^\circ 4' 18.042''$ and Dec = $-6^\circ 20' 43.19''$ near the bright tip/tilt star).

The OSIRIS data were reduced using standard infrared self-calibration techniques. First, the 36 individual frames were scaled to a common median and combined into a super-sky frame using a $3\text{-}\sigma$ clipped mean algorithm, masking out a $2'' \times 2''$ box around the location of the target source in each frame. This super-sky was divided by its own median in order to produce a super-flat-field image that was then used to flat-field the individual science frames. The median unmasked value was then subtracted from each flat-fielded science frame in order to produce the flat-fielded, foreground-subtracted science frames. These frames were then shifted by the dither offsets (adjusted slightly by hand to ensure proper alignment) and combined using a $3\text{-}\sigma$ clipped mean algorithm. The final image is shown in Figures 3 and 4.

The NIRC2 observations consist of 39 exposures of 80 s each in the K_s -band, 9 exposures of 120 s each in the H -band and 5 exposures of 300 s each in the J -band. Unfortunately, for the J -band data, there was an instrument problem during the night and only two of the frames were used in the end. We used the same tip-tilt star as above to do the AO corrections. The observations were carried out using the NIRC2 narrow camera with a field of view of $100'' \times 100''$ and a pixel scale of $0.01''/\text{pixel}$. We dithered each of the frames by $2''$ using a custom nine-point dithering pattern for better sky subtraction. To correct for flat-fielding and dark currents we acquired a set of ten dark frames and twenty dome flat frames. The dome flats were separated

into two sets with the first half with the dome flat lamp off and second half with the lamp on. The dome flat off frames were used to estimate the thermal radiation which is non-negligible for the K_s -band. The dome flat on frames were then subtracted with the combined flat-off map, and the individual dark and flat frames were combined to generate master dark and dome flat frames, respectively. This produced a combined dark-subtracted and flat-fielded images in the J , H and K_s bands. For each science exposure the sky background of each pixel were estimated by using the preceding and following images after bad pixels and the object it self had been masked. The reduction was carried out using custom python scripts. The images were then finally corrected for geometric distortion using IDL routines available on the NIRC2 webpage.

The NIRC2 J -band, Fig. 4D, provides the highest resolution image in our dataset of the system where the four SN images are visible. We used this image to determine the SN positions by fitting a model to the system. The lensing galaxy was modeled using a Sérsic profile (43) while Gaussians were used for the the SN images. The fitted SN positions are shown in Table S4.

Observations with the Wide-Field Camera 3 aboard the Hubble Space Telescope

The Hubble Space Telescope (HST) Wide Field Camera 3 (WFC3) images presented in Fig. 4 A–C were obtained under program DD 14862 (Principal Investigator: Goobar) using the ultra-violet and visual (UVIS) channel on 2016 Oct 24 in the $F475W$, $F625W$ and $F814W$ filters (where the filter names correspond to the central wavelengths in nm). UVIS consists of two thinned, backside illuminated, ultra violet optimized 2048×4096 pixel CCDs. However, only part of the UVIS2 chip was read for the iPTF16geu observations using the UVIS2-C512C-SUB aperture. UVIS has a pixel scale of $0.04''/\text{pixel}$ and the diffraction limited PSF for these filters results in an image quality of $\text{FWHM} \simeq 0.07''$. We used a standard 3-point dithering pattern with post-flash to maximize the charge transfer efficiency (CTE) during read-out. The total expo-

sure time for the three filters were 378 s, 291 s and 312 s for $F475W$, $F625W$ and $F814W$, respectively.

The images were automatically processed at the Space Telescope Science Institute first through version 3.3 of the `calwf3` pipeline where they are dark subtracted, flat-fielded and corrected for charge-transfer inefficiency. Further, the individual flatfielded images were combined and corrected for geometric distortion using the `AstroDrizzle` software.

Using the same model as for the SN image positions, we fitted the relative fluxes of SN images 2–4 with respect to image 1. For this procedure we kept the image positions fixed to the values in Table S4, while allowing for a shift and a rotation of the the whole model. For the $F625W$ band, which covers a similar wavelength range as the R -band, we found that 90 % of the total flux is contained in images 1–2 and 70 % of the total flux is contained in image 1 alone. The relative brightnesses for the SN images with respect to the brightest image 1, the relative reddening, and the extinction these correspond to assuming the extinction law from (23) are shown in Table S5.

Fitting to a SN Ia lightcurve template

The lightcurves from the P48 and P60 photometry are presented in Figs. 2, and S2. Since SNe Ia are a homogenous class of objects, templates or lightcurve models can typically be fitted to the data. The free parameters are the time, t_0 , and brightness, m_B^* , of maximum in the rest-frame B -band, the lightcurve width and the color of the SN.

The lightcurve width can be quantified by introducing a stretch factor, s , that scales the time variable of the template with respect to t_0 . It has been shown that same behavior is also captured by the second principal component of the SALT2 lightcurve model (17). In short, the SALT2 model is constructed from a principal component analysis of a large data set of normal SNe Ia. The eigenvalue for the first component is directly related to the peak brightness, m_B^* , while the

eigenvalue for the second component, x_1 , is normalized so that a SN with $x_1 = 0$ correspond to an average normal SN Ia. Further, objects with $x_1 = \pm 1$ have lightcurve widths that correspond to $\pm 1\sigma$ of normal SNe Ia lightcurve width distribution.

The color is typically defined in terms of the rest-frame $B - V$ magnitude. This is then used to scale a color, or extinction, law that describes how the flux ratios vary with wavelength. For a standard extinction law, the color excess, $E(B - V)$, is used to scale the law, where $E(B - V)$ is the $B - V$ magnitude deviation from what would have been measured in the absence of extinction. SALT2 uses an empirically derived color law where the scaling parameter, \mathcal{C} , is the deviation from the average $B - V$ rest-frame color.

We fitted both a lightcurve template and the SALT2 model to the P48 and P60 photometry. In Fig. 2 we show the best fitted SALT2 model. SALT2 was also used for the SN Ia cosmology sample presented in (20). Using the same model allows us to estimate the magnification independently of the value of the Hubble constant, H_0 , or any other cosmological parameter. The SALT2 model has four free parameters, for which we obtain, $t_0 = 57654.1 \pm 0.2$, $m_B^* = 19.12 \pm 0.03$, and $\mathcal{C} = 0.23 \pm 0.03$ and $x_1 = 0.08 \pm 0.19$, respectively. The corrected peak magnitude, m_B^{corr} , is further obtained as

$$m_B^{\text{corr}} = m_B^* - \beta \cdot \mathcal{C} + \alpha \cdot x_1$$

where $\beta = 3.101 \pm 0.075$ and $\alpha = 0.141 \pm 0.006$ have been derived simultaneously with the cosmological parameters by (20) from the full sample of 740 SNe Ia. Since their data set is well-sampled around $z = 0.4$, we can compare the lightcurve of iPTF16geu with the expected average for the same redshift. This is shown in Fig. 2 together with the intrinsic brightness dispersions of SNe Ia. By then comparing the derived peak magnitude of iPTF16geu with the expected for an unlensed SN Ia at $z = 0.409$, we find that the SN has been boosted by -4.3 ± 0.2 magnitudes where the intrinsic dispersion is accounted for in the quoted error bar.

We also tried to fit the spectral series of SN 2011fe, which is a normal and well observed SN Ia, to the data. In Fig. S2 we show both the SALT2 lightcurve model and the best SN 2011fe fit using the spectral series for the latter compiled by (44). The data are perfectly consistent with both models but SN 2011fe provides a better fit in the rest-frame U -band. However, since the SALT2 fit allows us to directly compare the brightness of iPTF16geu to other SNe Ia at the same redshift in a cosmology independent manner we decided to use this for the main analysis. iPTF16geu has the same lightcurve shape as SN2011fe, but a reddening of $E(B - V) = 0.31 \pm 0.05$ mag is required, assuming the extinction law from (23).

Both the SALT2 model and SN 2011fe fits show that the iPTF16geu is consistent with a normal and average SNe Ia, but the derived values of \mathcal{C} and $E(B - V)$ suggest that the SN is reddened by interstellar extinction. This reddening is taken into account for the estimated lensing magnification and uncertainty above. However, given that most of the measured light, $\sim 70\%$, is contained in SN image 1, the measured \mathcal{C} is dominated by the color of this image. Since we have also measured differential reddening of images 2–4 with respect to SN image 1, the magnification of the system could in fact be higher. If the measured differential extinction from Table S5 is taken into account we find that the total magnification of the system lie in the range -4.1 mag to -4.8 mag.

Modelling of the gravitational lens

Our default lens model is an isothermal ellipsoid galaxy (25, 26) for which the convergence is given by

$$\kappa = \frac{b}{2\omega}, \quad (\text{S1})$$

where b is a convergence normalization parameter and

$$\omega^2 = (1 - \epsilon)(x - x_0)^2 + (1 + \epsilon)(y - y_0)^2. \quad (\text{S2})$$

Here, x_0 and y_0 correspond to the position of the lens centre and $(1 + \epsilon)/(1 - \epsilon)$ is the major-to-minor axis ratio. The magnification is given by (26)

$$\mu(x_1, x_2) = \left(1 - \frac{b}{\omega}\right)^{-1}, \quad (\text{S3})$$

i.e., the isodensity contour $\kappa = 1/2$ correspond to the critical line in the lens plane. In the forthcoming, positions in the lens plane are given in angular units. In terms of ϵ , the ellipticity, ϵ_e , of the galaxy is given by

$$\epsilon_e = 1 - \sqrt{\frac{1 - \epsilon}{1 + \epsilon}}. \quad (\text{S4})$$

The projected mass M inside an isodensity contour of constant ω is given by (26)

$$M = \frac{c^2}{4G} \frac{D_s D_l}{D_{ls}} \frac{b\omega}{\sqrt{1 - \epsilon^2}}. \quad (\text{S5})$$

Assuming cosmological parameter values of $H_0 = 67.8 \text{ km s}^{-1} \text{ Mpc}^{-1}$ and $\Omega_M = 0.308$ and zero spatial curvature (45),

$$D_l = 745.8 \text{ Mpc}, D_s = 1157.0 \text{ Mpc}, \text{ and } D_{ls} = 513.2 \text{ Mpc},$$

where D_l is the angular diameter distance to the lens, D_s to the source and D_{ls} between the lens and the source. The mass inside the critical line where $\omega = b$ is

$$M = \left(\frac{b}{1''}\right)^2 \frac{2.0 \cdot 10^{11} M_\odot}{\sqrt{1 - \epsilon^2}}. \quad (\text{S6})$$

Using the `lensmodel` software (46, 47), we fit the model to the observed SN positions by varying b , ϵ , the position angle ϕ (from North to East) of the major axis, and the offset, $(\Delta\alpha, \Delta\delta)$, between the center of the lens model and the Sérsic profile used to fit the observed light of the lensing galaxy as described above. The results are

$$\begin{aligned} b &= 0.287'' \pm 0.005'', \\ \Delta\alpha &= -0.013'' \pm 0.007'', \end{aligned}$$

$$\begin{aligned}
\Delta\delta &= -0.004'' \pm 0.008'', \\
\epsilon &= 0.16 \pm 0.09, \\
\phi &= 65.8 \pm 0.9,
\end{aligned}$$

or

$$M = (1.69 \pm 0.06) \cdot 10^{10} M_{\odot}, \quad (\text{S7})$$

$$\epsilon_e = 0.15 \pm 0.07. \quad (\text{S8})$$

For the best fit parameter values we get $\chi_{\min}^2 = 0.022$. Constraining the centre of the lens to coincide with the maximum surface brightness of the lens galaxy, i.e. $(\Delta\alpha, \Delta\delta) = (0, 0)$ within the observational uncertainties, i.e., $\pm 0.008''$, the minimum χ^2 increases to $\chi_{\min}^2 = 1.8$. Following (30), we calculate the velocity dispersion by averaging over all possible inclination angles and intrinsic axis ratios that can give rise to the observed projected surface density. The resulting relation between b and the velocity dispersion, σ_v , is given by

$$b = 4\pi \left(\frac{\sigma_v^2}{c^2} \right)^2 \frac{D_{ls}}{D_s} \sqrt{1 - \epsilon} \lambda \left(\sqrt{\frac{1 - \epsilon}{1 + \epsilon}} \right), \quad (\text{S9})$$

where the functional form of λ depends on the probability for the three dimensional mass distribution of the lens to be oblate or prolate. Assuming total ignorance of this probability, we can read off the value of λ for $\epsilon = 0.16$ from figure 1 in (30) to be $\lambda = 1 \pm 0.05$. Numerically, we have

$$\sigma_v = 280 \left(\frac{b}{\lambda} \sqrt{1 - \epsilon} \right)^{\frac{1}{2}} \text{ km s}^{-1} = 156 \pm 4 \text{ km s}^{-1},$$

where $\lambda\sqrt{1 - \epsilon} = 0.92 \pm 0.04$.

We calculate the expected flux ratios, r , and their associated uncertainties by taking a weighted average of the flux ratios over a grid of parameter values, here denoted by index

i ,

$$\bar{r} = \sum_i \mathcal{L}_i r_i, \quad (\text{S10})$$

$$\sigma_{\bar{r}}^2 = \sum_i \mathcal{L}_i (r_i - \bar{r})^2, \quad (\text{S11})$$

where the weight is given by the likelihood of the parameter values given the observed image positions,

$$\mathcal{L}_i \equiv \exp\left(-\frac{1}{2}\chi_i^2\right) / \sum_i \exp\left(-\frac{1}{2}\chi_i^2\right). \quad (\text{S12})$$

Suppressing the bar as an indicator for average values, the magnitude differences $\Delta m_{ij} = -2.5 \ln f_i/f_j$ between images i and j are:

$$\begin{aligned} \Delta m_{12} &= -0.39 \pm 0.11, & \Delta m_{13} &= -0.33 \pm 0.06, & \Delta m_{14} &= 0.73 \pm 0.06, \\ \Delta m_{23} &= 0.04 \pm 0.11, & \Delta m_{24} &= 1.11 \pm 0.06, & \Delta m_{34} &= 1.06 \pm 0.06. \end{aligned}$$

In conclusion, image 4 is expected to be the brightest, while it is in fact observed to be the faintest.

The predicted time delay, calculated as weighted averages analogously to the flux ratios, between the SN images is small, ranging from 1.9 ± 1.2 hours to 15.7 ± 6.3 hours. Thus, the maximal time-delay between any two images is 35 hours at the 99.9% confidence level with the adopted model.

While the model estimates of the magnitude differences among the SN images have small uncertainties, the total magnification is poorly constrained. Since there is a tail of very high magnification output compatible with the observed image positions, the resulting weighted mean total magnification is very sensitive to details of the grid of parameter values and possible cuts of low probability parameter values. Only when disregarding all parameter values not being within 2σ of the best fit parameters can the total magnification be constrained at all, $\mu_{\text{tot}} = 43 \pm 29$, consistent with the observed magnification $\mu \sim 52$.

Motivated by the discrepancy between the image magnitude differences observed and the ones predicted by the smooth lensing model, we consider the possibility of sub-structures as possible added contributors to the lensing of one or more SN images.

Such sub-structures can include galactic subhalos (52), and compact objects in the form of stars or possible compact dark matter objects. The magnification of SNe from stars is studied in (53), where it is found that $\sim 70\%$ of multiple lensed SNe will experience additional magnification from the lens galaxy star population of > 0.5 mag. The case of lensed quasars is studied in, e.g (54).

A population of compact objects will create a network of caustics that can give rise to large magnifications if the source size is sufficiently small. If there is a relative motion between the source, observer and the lensing compact object, or if the source size is changing, the magnification can vary. The time scale of the variations will typically correspond to the Einstein radius crossing time (see below), but can also be shorter in the case of caustic crossing events (55).

A full treatment of the gravitational lensing effects of sub-structures is beyond the scope of this paper, but in order to show the typical scales involved, we briefly study the lensing effect of a single compact object.

In the isolated point mass lens approximation, the relevant source plane length scale is given by (48)

$$\eta_0 = \sqrt{2R_S \frac{D_s D_{ls}}{D_l}} = \sqrt{\frac{M}{M_\odot}} \times 3.8 \cdot 10^{16} \text{ cm}, \quad (\text{S13})$$

where R_S is the Schwarzschild radius of the lens. To act efficiently as a lens, η_0 should be larger than the physical size, R , of the Type Ia SNe photosphere, typically

$$\frac{R}{10^{15} \text{ cm}} \sim 2.0 + 0.62 \frac{(t - t_{\text{max}})}{1 \text{ week}}, \quad (\text{S14})$$

which is derived from the the measured expansion velocities of the photosphere of SN2011fe (22, 49).

A single lens point mass should have $M \gtrsim 0.12 M_{\odot}$ to be effective also one month after maximum. For a lens with velocity 156 km s^{-1} , this corresponds to time scales greater than 9 years. We can thus neglect any time dependence induced to the lightcurve from the motion of isolated point masses with $M \gtrsim 0.12 M_{\odot}$.

Predicted rate of highly magnified SNe Ia in iPTF

To date, almost 2000 SNe Ia up to $z \sim 0.2$ have been discovered at P48 and classified over a period of eight years (945 observing nights), with a detection limit of $R \sim 21 \text{ mag}$. Since they are brighter, lensed SNe can be observed to higher redshifts. Using the compilation of measured SN Ia volumetric rates in (*I*, see their Fig. 2), we estimate that within the larger volume up to $z = 0.4$, the number of SNe Ia explosions is $12.6 \text{ deg}^{-2} \text{ year}^{-1}$, which when combined with the total monitoring time and the average solid angle of the survey, yields a total of 6×10^4 SNe Ia in the field of view. This corresponds to a relative fraction 1.7×10^{-5} for events like iPTF16geu, if this single event is representative for the true rate. Estimates of the inefficiencies in transient detection and spectroscopic typing over the lifetime of the survey have been included in the calculation.

To compare this outcome with the estimate of the expected probability we use the ray-tracing SNOC Monte-Carlo package (*50*). SNOC was used in (*11*) to assess the expected rate of strongly lensed SNe in planned satellite missions. We run a total of 10^7 simulated lines-of-sight up to $z = 0.45$, with a volumetric redshift dependent SN Ia rate following the star formation rate with redshift, one of the options in SNOC. The matter spatial distribution in galaxy halos along the line of sight are simulated with two different smooth spherical functions, the Singular Isothermal Sphere (SIS) profile,

$$\rho(r) = \frac{\sigma_v^2}{2\pi G r^2},$$

where σ_v^2 is the velocity dispersion; and the NFW profile (51),

$$\rho(r) = \frac{\rho_0}{\frac{r}{R_s} \left(1 + \frac{r}{R_s}\right)^2},$$

where ρ_0 and R_s parameters of the model and vary between halos. Since we only consider spherical profiles, our simulations will not produce four, but only two images. Furthermore, these simulations do not include the contribution from microlensing by a stellar population in the line of sight.

However, in addition to the smooth spherical functions, we tested adding contributions from point-like lenses (POI) to the mass density. In all cases, the contributions to the mass density is self-consistently normalised to give the cosmological average mass density of the universe found by the Planck collaboration for a Λ CDM universe, $\Omega_M = 0.308$ (45). The resulting distribution of the expected gravitational lensing amplification for the iPTF survey, μ , can be seen in Fig. S3. For the simulations with smooth distributions, e.g., NFW, no event like iPTF16geu came out of the simulations, corresponding to a probability less than 10^{-3} . Adding substructures in the form of compact objects increases the chances of intersecting a lens, yet the high magnification found for iPTF16geu is rare. For a 90% contribution of compact objects to the cosmic mass density, Ω_M , we find a 5% chance of discovering a SN Ia with comparable lensing magnification within the limited redshift range probed. In conclusion, the lensing characteristics of iPTF16geu are rather unlikely, even considering the possibility of having a high density of discrete compact sources.

Table S1: **Imaging of iPTF16geu.** All observations where imaging data of iPTF16geu were obtained.

UTC Civil date	MJD (days)	Telescope	Filter	Exp. time (s)
2016 Sep 05.3	57636.33	P48	<i>R</i>	60
2016 Sep 06.2	57637.18	P48	<i>R</i>	120

Continued on next page

UTC Civil date	MJD (days)	Telescope	Filter	Exp. time (s)
2016 Sep 07.2	57638.18	P48	R	120
2016 Sep 08.2	57639.23	P48	R	120
2016 Sep 09.2	57640.21	P48	R	120
2016 Sep 10.2	57641.20	P48	R	120
2016 Sep 11.2	57642.20	P48	R	120
2016 Sep 15.3	57646.33	P60/RC	r'	90
2016 Sep 15.3	57646.33	P60/RC	i'	90
2016 Sep 15.3	57646.33	P60/RC	g'	90
2016 Sep 17.4	57648.36	P60/RC	r'	90
2016 Sep 17.4	57648.36	P60/RC	i'	90
2016 Sep 17.4	57648.36	P60/RC	g'	90
2016 Sep 23.1	57654.14	P48	R	60
2016 Sep 24.1	57655.11	P48	R	120
2016 Sep 25.1	57656.12	P48	R	120
2016 Sep 26.1	57657.15	P48	R	120
2016 Sep 27.1	57658.13	P48	R	120
2016 Sep 28.2	57659.25	P48	R	60
2016 Sep 29.1	57660.15	P48	R	60
2016 Sep 30.1	57661.11	P48	R	120
2016 Oct 01.1	57662.10	P48	R	120
2016 Oct 02.1	57663.12	P48	R	120
2016 Oct 03.2	57664.17	P48	R	60
2016 Oct 03.2	57664.25	P60/RC	r'	90
2016 Oct 03.3	57664.25	P60/RC	i'	90
2016 Oct 03.3	57664.26	P60/RC	r'	90
2016 Oct 03.3	57664.26	P60/RC	i'	90
2016 Oct 03.3	57664.26	P60/RC	g'	90
2016 Oct 04.3	57665.29	P60/RC	r'	90
2016 Oct 04.3	57665.30	P60/RC	i'	90
2016 Oct 04.3	57665.30	P60/RC	g'	90
2016 Oct 06.1	57667.11	P60/RC	r'	90
2016 Oct 07.1	57668.10	P48	R	120
2016 Oct 08.1	57669.11	P48	R	60
2016 Oct 08.1	57669.15	P60/RC	r'	90
2016 Oct 09.1	57670.10	P48	R	60
2016 Oct 09.2	57670.17	P60/RC	r'	90
2016 Oct 09.2	57670.17	P60/RC	i'	90
2016 Oct 09.2	57670.17	P60/RC	g'	90
2016 Oct 09.2	57670.22	P60/RC	r'	90
2016 Oct 09.2	57670.23	P60/RC	i'	90
2016 Oct 10.2	57671.22	P60/RC	i'	90
2016 Oct 10.2	57671.24	P60/RC	r'	90
2016 Oct 10.2	57671.24	P60/RC	i'	90
2016 Oct 11.1	57672.05	VLT/NACO	K_s	6960
2016 Oct 12.2	57673.19	P60/RC	r'	90
2016 Oct 12.2	57673.19	P60/RC	i'	90

Continued on next page

UTC Civil date	MJD (days)	Telescope	Filter	Exp. time (s)
2016 Oct 12.2	57673.21	P60/RC	r'	90
2016 Oct 12.2	57673.21	P60/RC	i'	90
2016 Oct 13.1	57674.12	P60/RC	r'	90
2016 Oct 13.1	57674.12	P60/RC	i'	90
2016 Oct 13.2	57674.21	Keck/OSIRIS	H_{bb}	1080
2016 Oct 13.2	57674.21	P60/RC	r'	90
2016 Oct 13.2	57674.21	P60/RC	i'	90
2016 Oct 22.2	57683.22	Keck/NIRC2	K_s	3120
2016 Oct 23.2	57684.22	Keck/NIRC2	H	1080
2016 Oct 24.9	57685.88	HST/WFC3	$F625W$	291
2016 Oct 24.9	57685.89	HST/WFC3	$F814W$	312
2016 Oct 24.9	57685.92	HST/WFC3	$F475W$	378
2016 Nov 05.2	57697.21	Keck/NIRC2	J	600

Table S2: **Photometry of individual exposures of iPTF16geu from the P48 and P60/RC observations listed in Table S1. The photometry is given in flux, f , which can be converted to magnitudes, m , in the AB system as $m = -2.5 \log_{10}(f) + ZP$, with $ZP = 25$.**

UTC Civil date	MJD (days)	Telescope	Filter	Flux (arbitrary)	Flux σ	ZP (AB)
2016 Aug 31.3	57631.33	P48	R	19	10	25.0
2016 Sep 01.3	57632.32	P48	R	8	13	25.0
2016 Sep 02.4	57633.35	P48	R	17	8	25.0
2016 Sep 04.3	57635.33	P48	R	38	10	25.0
2016 Sep 05.3	57636.33	P48	R	52	10	25.0
2016 Sep 06.2	57637.18	P48	R	81	13	25.0
2016 Sep 06.3	57637.33	P48	R	84	12	25.0
2016 Sep 07.2	57638.18	P48	R	98	11	25.0
2016 Sep 07.3	57638.33	P48	R	86	11	25.0
2016 Sep 08.2	57639.23	P48	R	115	14	25.0
2016 Sep 08.3	57639.34	P48	R	110	10	25.0
2016 Sep 09.2	57640.21	P48	R	131	13	25.0
2016 Sep 09.3	57640.32	P48	R	131	13	25.0
2016 Sep 10.2	57641.20	P48	R	166	18	25.0
2016 Sep 10.3	57641.32	P48	R	153	13	25.0
2016 Sep 11.2	57642.20	P48	R	205	19	25.0
2016 Sep 11.3	57642.31	P48	R	177	18	25.0
2016 Sep 15.3	57646.33	P60/RC	r'	221	16	25.0
2016 Sep 15.3	57646.33	P60/RC	i'	278	10	25.0
2016 Sep 15.3	57646.33	P60/RC	g'	107	13	25.0
2016 Sep 17.4	57648.36	P60/RC	r'	270	37	25.0
2016 Sep 17.4	57648.36	P60/RC	i'	325	18	25.0

Continued on next page

UTC Civil date	MJD (days)	Telescope	Filter	Flux (arbitrary)	Flux σ	ZP (AB)
2016 Sep 17.4	57648.36	P60/RC	g'	112	16	25.0
2016 Sep 23.1	57654.14	P48	R	288	19	25.0
2016 Sep 24.1	57655.11	P48	R	283	23	25.0
2016 Sep 24.2	57655.24	P48	R	283	18	25.0
2016 Sep 25.1	57656.12	P48	R	310	23	25.0
2016 Sep 25.2	57656.25	P48	R	278	20	25.0
2016 Sep 26.1	57657.15	P48	R	273	18	25.0
2016 Sep 26.2	57657.25	P48	R	270	25	25.0
2016 Sep 27.1	57658.13	P48	R	281	21	25.0
2016 Sep 27.2	57658.18	P48	R	273	18	25.0
2016 Sep 28.2	57659.25	P48	R	286	24	25.0
2016 Sep 29.1	57660.15	P48	R	251	21	25.0
2016 Sep 30.1	57661.11	P48	R	247	20	25.0
2016 Sep 30.2	57661.15	P48	R	231	19	25.0
2016 Oct 01.1	57662.10	P48	R	265	27	25.0
2016 Oct 01.2	57662.23	P48	R	238	18	25.0
2016 Oct 02.1	57663.12	P48	R	227	17	25.0
2016 Oct 02.2	57663.22	P48	R	225	19	25.0
2016 Oct 03.2	57664.17	P48	R	229	19	25.0
2016 Oct 03.2	57664.25	P60/RC	r'	223	18	25.0
2016 Oct 03.3	57664.25	P60/RC	i'	347	29	25.0
2016 Oct 03.3	57664.26	P60/RC	r'	236	13	25.0
2016 Oct 03.3	57664.26	P60/RC	i'	316	55	25.0
2016 Oct 03.3	57664.26	P60/RC	g'	48	8	25.0
2016 Oct 04.3	57665.29	P60/RC	r'	205	19	25.0
2016 Oct 04.3	57665.30	P60/RC	i'	319	91	25.0
2016 Oct 04.3	57665.30	P60/RC	g'	53	8	25.0
2016 Oct 06.1	57667.11	P60/RC	r'	192	37	25.0
2016 Oct 07.1	57668.10	P48	R	203	19	25.0
2016 Oct 07.2	57668.22	P48	R	191	18	25.0
2016 Oct 08.1	57669.11	P48	R	180	23	25.0
2016 Oct 08.1	57669.15	P60/RC	r'	145	27	25.0
2016 Oct 09.1	57670.10	P48	R	194	25	25.0
2016 Oct 09.2	57670.17	P60/RC	r'	163	6	25.0
2016 Oct 09.2	57670.17	P60/RC	i'	251	12	25.0
2016 Oct 09.2	57670.17	P60/RC	g'	25	4	25.0
2016 Oct 09.2	57670.22	P60/RC	r'	146	12	25.0
2016 Oct 09.2	57670.23	P60/RC	i'	244	52	25.0
2016 Oct 10.2	57671.22	P60/RC	i'	227	368	25.0
2016 Oct 10.2	57671.24	P60/RC	r'	126	13	25.0
2016 Oct 10.2	57671.24	P60/RC	i'	242	187	25.0
2016 Oct 12.2	57673.19	P60/RC	r'	120	135	25.0
2016 Oct 12.2	57673.19	P60/RC	i'	223	29	25.0
2016 Oct 12.2	57673.21	P60/RC	r'	118	13	25.0
2016 Oct 12.2	57673.21	P60/RC	i'	256	141	25.0
2016 Oct 13.1	57674.12	P60/RC	r'	132	18	25.0
2016 Oct 13.1	57674.12	P60/RC	i'	203	11	25.0

Continued on next page

UTC Civil date	MJD (days)	Telescope	Filter	Flux (arbitrary)	Flux σ	ZP (AB)
2016 Oct 13.2	57674.21	P60/RC	r'	96	12	25.0
2016 Oct 13.2	57674.21	P60/RC	i'	238	79	25.0

Table S3: **Spectroscopic observations of iPTF16geu used for identification and redshift measurements.**

UT Date	MJD (days)	Phase (days)	Telescope Instrument	R ($\lambda/\Delta\lambda$)	$\Delta\lambda$ (\AA)	λ range (\AA)	Exp. time (s)	Airmass
Oct 2.23	57663.23	6.5	P60/SEDMM	100	58	4000-9500	2700	1.43
Oct 4.22	57665.22	7.9	P200/DBSP	740	8	3300-10000	1800	1.37
Oct 6.13	57667.13	9.3	P200/DBSP	560	10	3300-10000	3600	1.51
Oct 9.90	57670.90	12.0	NOT/ALFOSC	360	16	3500-9600	2700	1.22

Table S4: **Fitted relative SN image positions.** The positions are given in polar coordinates with respect to the center, of the Sérsic profile, and the angle, $-\pi < \phi \leq \pi$, is defined from West to North. The SN image numbers are shown in Fig. 4. The fitted statistical uncertainty on r and are ϕ 0.001'' and 0.004 rad, respectively. The uncertainty, in the position of the whole system, i.e. the center of the Sérsic profile is 0.008'' in both x and y .

SN Image	r (arcsec)	ϕ (rad)
1	0.2679	+1.7861
2	0.3133	-2.7252
3	0.2874	-0.9761
4	0.2803	+0.4554

Table S5: **Relative photometry with respect to the first SN image.** Here, $E(F625W - F814W)$, is the relative color color excess with respect to SN image 1. All quoted uncertainties are statistical errors. In the last two columns, the relative extinction are given using the measured $E(F625W - F814W)$ together with the extinction law from (23).

SN image	$\Delta F625W$ (mag)	$\Delta F814W$ (mag)	$E(F625W - F814W)$ (mag)	A_{F625W} (mag)	A_{F814W} (mag)
2	1.26(0.01)	1.12(0.01)	0.14(0.01)	0.5	0.4
3	2.46(0.02)	2.33(0.02)	0.12(0.03)	0.5	0.4
4	3.62(0.05)	2.88(0.03)	0.75(0.06)	2.8	2.1

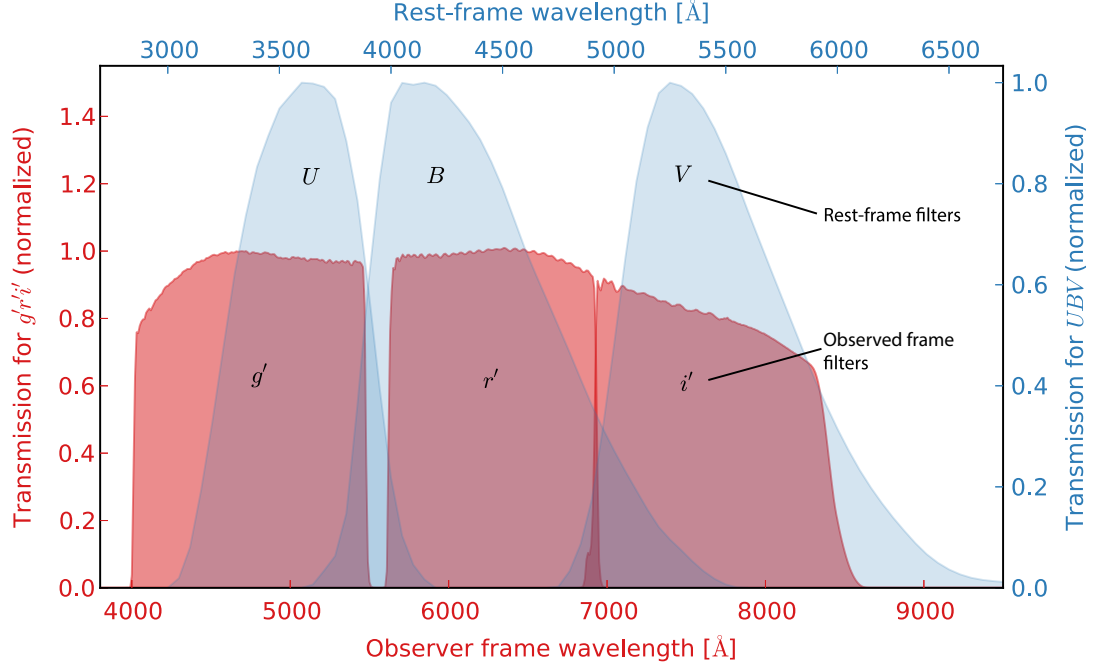


Figure S1: **Comparison between the observer frame P60 RC filters and the rest-frame standard filters UBV , which historically have been used for studying SNe Ia..** The relative transmissions of the observer frame P60 $g'r'i'$ filters are shown in red for the wavelengths indicated by the bottom horizontal axis, while the corresponding rest-frame wavelengths and UBV filter transmissions are plotted in blue. It is clear from the figure that the observer frame RC $g'r'i'$ filters provide a close match to the rest-frame UBV for the redshift $z_{SN} = 0.409$.

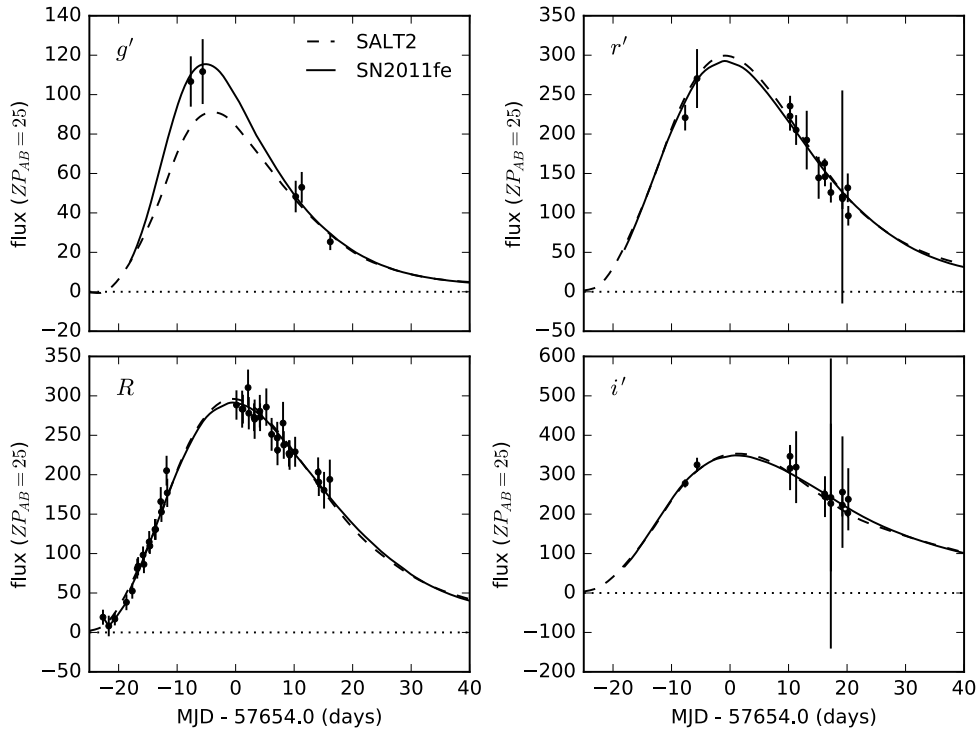


Figure S2: **Lightcurves of iPTF16geu in the P48 R -band and the P60 RC $g'r'i'$ bands.** The error bars are correlated. The solid lines show the fit of the nearby and normal SN 2011fe, while the dashed show the best fit using the SALT2 model. The lightcurve fitting is carried out in linear flux space which appropriately allows the inclusion of low signal-to-noise and negative flux measurements. These points have been omitted in the plotting of Fig. 2, which shows magnitudes, while all data are shown here. The individual fluxes are given in Table S2.

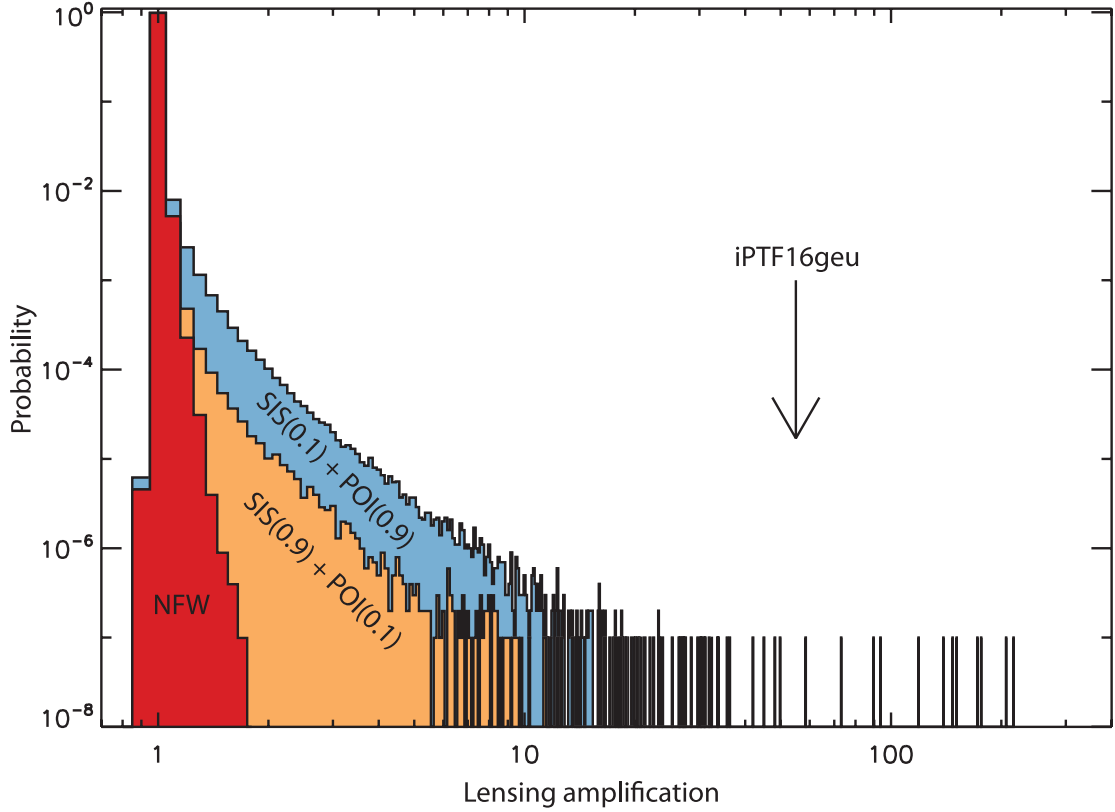


Figure S3: **Computation of the lensing probability for SNe Ia in the Palomar Transient Factory survey.** SNOC simulations (50) of the expected likelihood for the gravitational lensing amplification of SNe Ia up to $z = 0.45$ as a function of the density distribution of matter in galaxy halos. The three cases displayed correspond to a smooth NFW profile, and a SIS profile with a 10% and 90% fraction of substructures in the form of point-like lenses (POI). Only simulations with substructures provide a non-vanishing probability of finding an event with as high amplification as iPTF16geu, indicated by the arrow.